

Article

Structure and Thermoelectric Characterization of p-Type SnTe Nanobulk Material Synthesized by Charge Compensation Chemical Reaction

Ryosuke Fujiwara, Yuta Ikeda, Takuto Kawaguchi, Yohei Takashima , Takaaki Tsuruoka 
and Kensuke Akamatsu * 

Department of Nanobiochemistry, Frontiers of Innovative Research in Science and Technology (FIRST),
Konan University, 7-1-20 Minatojima-minamimachi, Chuo-ku, Kobe 650-0047, Japan

* Correspondence: akamatsu@konan-u.ac.jp

Abstract: SnTe is the most widely studied p-type thermoelectric (TE) alternative to PbTe. In this study, we prepared a nanostructured SnTe bulk material via spark plasma sintering from a precursor synthesized by a chemical precipitation process without using organic molecules. The sintered sample comprised tiny grains (100–300 nm) with high-density grain boundaries. Eventually, because the material would contain no impurities acting as scattering nodes of charge carriers, the material exhibited a relatively high electrical conductivity of $7.07 \times 10^5 \text{ Sm}^{-1}$ at 310 K. The material demonstrated low lattice thermal conductivity ($0.87 \text{ Wm}^{-1}\text{K}^{-1}$ at 764 K), which can be owing to the increasing phonon scattering at grain boundaries. The maximum ZT was 0.31 at 764 K in the measured temperature range. This study provides a method for the design of phase-pure and surfactant-free SnTe thermoelectric materials that exhibit low lattice thermal conductivity and high carrier mobility using a chemical synthetic approach.

Keywords: thermoelectric material; tin telluride; chemical precipitation; low lattice thermal conductivity



Citation: Fujiwara, R.; Ikeda, Y.; Kawaguchi, T.; Takashima, Y.; Tsuruoka, T.; Akamatsu, K. Structure and Thermoelectric Characterization of p-Type SnTe Nanobulk Material Synthesized by Charge Compensation Chemical Reaction. *Energies* **2024**, *17*, 190. <https://doi.org/10.3390/en17010190>

Academic Editor: Huang Zhang

Received: 15 November 2023

Revised: 25 December 2023

Accepted: 27 December 2023

Published: 29 December 2023



Copyright: © 2023 by the authors. Licensee MDPI, Basel, Switzerland. This article is an open access article distributed under the terms and conditions of the Creative Commons Attribution (CC BY) license (<https://creativecommons.org/licenses/by/4.0/>).

1. Introduction

With the increasing attention to environmental concerns, developing clean energy-supplying technologies is essential. Thermoelectric (TE) power generation, which can directly convert waste heat into electricity, has attracted considerable attention as a suitable technique [1–3]. The TE performance of materials is generally determined by the dimensionless figure of merit, $ZT = S^2\sigma T / (\kappa_{ele} + \kappa_{lat})$, where S , σ , T , κ_{ele} , and κ_{lat} are the Seebeck coefficient, the electrical conductivity, the absolute temperature, electrical thermal conductivity, and lattice thermal conductivity, respectively [4]. However, the interdependence between S , σ , and κ_{ele} limits the improvement of ZT [4].

To date, several groups have reported various lead-chalcogenide-based materials with high ZT near the mid-temperature range [5–8]. Several PbTe-based materials demonstrated excellent ZT above 2.0 [6,7]. However, owing to the high toxicity of lead to the environment, the use of lead-chalcogenide-based compounds in TE power generators is considerably limited [9,10]. Therefore, several researchers have explored new lead-free materials with low toxicity. Recently, SnTe has been proposed as a promising Pb-free alternative material because its crystal and band structures of SnTe and PbTe are similar [10–12]. However, because SnTe has a low-energy band gap between the valence and conduction bands (~0.18 eV), it has a high hole concentration (nH) owing to bipolar effects, which leads to low S and high k_{ele} . In addition, due to the large energy separation between the valence bands of light and heavy holes (0.3–0.4 eV), the heavy holes in the valence band do not contribute to charge transport, further reducing S [13–15]. Furthermore, because the atomic mass of Sn is lighter than that of Pb, SnTe exhibits a higher k_{lat} compared to that of PbTe [13]. Therefore, the SnTe ingot exhibits a low ZT (<0.3 near 800 K) [11].

To date, several approaches for improving the ZT for SnTe materials have been reported, including band engineering and defect engineering [12]. Band engineering is a strategy to improve the Seebeck coefficient by modifying the band structure, and SnTe has been doped with various elements, such as I [16], Mn [17–19], In [20], Mg [21], Ge [22], Ca [23], and Cu [24], achieving the maximum $ZT = \sim 1.2$ at ~ 900 K [17–25]. Further, defect engineering is a strategy to decrease the lattice thermal conductivity based on the phonon scattering effect, which is achieved by miniaturizing the crystallite size of materials, i.e., increasing the density of grain boundaries [12,26–30]. Generally, SnTe materials with tiny grains are prepared via mechanical methods combining melting, ball-milling, and sintering [29–31]. However, the size of grains obtained via mechanical methods is more than several tens of micrometers [31] and further densification of the grain boundaries is challenging. In addition, high-energy mechanical alloying processes can cause elemental losses in SnTe, leading to a high carrier concentration and low carrier mobility [29]. Recently, wet chemical synthesis processes such as microwave [32], solvothermal [15,33], and wet-chemical methods [13,34,35] have been reported that directly synthesize SnTe nanocrystals. Organic molecules are commonly used as complexing agents, protectants, and surfactants to prepare small crystals in solution [13,34]. However, the molecules were adsorbed onto the surface of the obtained nanocrystals and incorporated into the resulting bulk materials [26]. In addition, wet chemical synthesis processes are usually performed at a higher temperature for longer reaction times, and the crystal size of materials prepared by these processes is usually ~ 10 μm [13–15,34]. These issues significantly reduce the electrical conductivity and make it difficult to reduce the lattice thermal conductivity [26]. Therefore, developing a synthetic strategy for SnTe materials with high-density grain boundaries and without impurity phases to improve TE performance is essential.

In this study, we prepared a pure SnTe thermoelectric bulk material with nanosized grains by sintering a SnTe nanocrystal precursor that were synthesized via a chemical precipitation process without using organic molecules. Because the obtained material did not contain any organic molecules, it exhibited high carrier mobility, leading to high electrical conductivity. In addition, because the sintered sample comprised dense grain boundaries, phonon scattering can be induced, and the lattice thermal conductivity significantly decreases ($0.87 \text{ W m}^{-1} \text{ K}^{-1}$ at 764 K). Eventually, a maximum ZT of 0.31 was achieved at 764 K in the measurement temperature range. The present process can be effective and useful for developing SnTe nanostructured bulk materials with high thermoelectric performance.

2. Experimental

2.1. Chemicals

To synthesize a SnTe bulk material, tin (II) chloride dihydrate ($\text{SnCl}_2 \cdot 2\text{H}_2\text{O}$, Wako Pure Chemical Industries Ltd., Osaka, Japan, 96.0%) and Te powders (Kojundo Chemical Lab. Co., Ltd., Saitama, Japan, 45 μm pass, 99.999%) were used as raw materials. Acetic acid ($\text{C}_2\text{H}_4\text{O}_2$, Wako Pure Chemical Industries Ltd., 99.7%) was used to stably dissolve tin (II) sulfate in degassed water. Sodium borohydride (NaBH_4 , Wako Pure Chemical Industries Ltd., 95%) was used as reducing agent for the Te powder. 1-Decanol ($\text{C}_{10}\text{H}_{22}\text{O}$, Tokyo Chemical Industry Co., Ltd., Tokyo, Japan, >98%) was selected as the solvent and used for annealing for the as-synthesized powders.

2.2. Synthesis of SnTe Nanocrystal Precursor

Based on the procedure reported in our previous studies [36,37], precursor nanocrystals of the binary thermoelectric material SnTe were chemically synthesized in this study. All fabrication processes for SnTe thermoelectric material generation were performed under an Ar gas. SnCl_2 (48.72 mmol) was mixed with 1.95 L of degassed acetic acid aqueous solution (2 M) in Ar with stirring to prepare Sn^{2+} solution. Meanwhile, 48.72 mmol of Te powder and 194.9 mmol of solid NaBH_4 powders were placed in a flask in Ar, and 180 mL of degassed water cooled on ice was added to the flask under Ar gas flow. The solution was stirred for 2 h while cooling with water to reduce the Te powder, resulting in white

suspension. Then, 180 mL of degassed water was added into the suspension and stirred for 30 min to obtain transparent solution, forming a solution containing Te^{2-} . Thereafter, the solution was injected into the solution containing Sn^{2+} , resulting in rapid precipitation of black powders. After 5 min, the precipitate was washed repeatedly with a large amount of degassed water and degassed ethanol and dried under Ar flow under ultrasonication. The products were further dried at 60 °C for 12 h under vacuum, obtaining the black powder. The powder was then annealed in 1-decanol to improve its crystallinity. The obtained powder (11.5 g) was placed in a flask, and 800 mL of degassed 1-decanol was added into the flask under Ar. The flask was heated and refluxed at 506 K (the boiling point of the 1-decanol) for 24 h with vigorous stirring. The annealed powder was again washed with degassed water and, finally, degassed ethanol. The annealed powder was then dried by ultrasonication under Ar flow and further dried at 150 °C for 15 h under vacuum, obtaining the SnTe precursor nanocrystals.

2.3. Spark Plasma Sintering

The precursor was sintered to prepare the nanobulk material by spark plasma sintering (SPS, SPS-211Lx, Fuji Electronic Ind. Co., Saitama, Japan) at 723 K under a pressure of 60 MPa in vacuum, and the holding time at 723 K was 2 min. A graphite sheet was used in a 10.5 mm-diameter graphite die as a cover. The precursor (7.5 g) was loaded into a die sealed using graphite sheets (ϕ 10 mm), an Al_2O_3 disk (ϕ 10 mm), and graphite punches in a glove box.

2.4. Characterization

Transmission electron microscopy (TEM; JEM-1400, JEOL, operation voltage: 120 kV) was performed to observe the morphology of samples. The precursor and sintered samples were characterized using X-ray diffraction (XRD, RINT-2200 Ultima IV, Rigaku), scanning electron microscopy (SEM, JSM-7001FA, JEOL, operated at 15 kV), and energy-dispersive X-ray spectroscopy (SEM-EDX) to observe the crystal structure, morphology, and distribution of Sn and Te atoms. XRD was operated at 40 kV/50 mA using Cu-K α radiation ($\lambda = 1.542 \text{ \AA}$) in the range of $2\theta = 10\text{--}90^\circ$ with a scanning speed of $0.5^\circ \text{ min}^{-1}$. The lattice parameters of the precursor and sintered sample were calculated from the XRD patterns using Cohen's least-squares method. Additionally, the crystallite size and micro-strain of the sintered sample were derived from the Williamson–Hall plot. X-ray photoelectron spectroscopy (XPS, JPS-9010MC, JEOL, Mg-K α) analysis was performed to determine the chemical states of the sintered SnTe sample. The chemical composition and metal content of the sintered sample were evaluated from inductively coupled plasma (ICP, SPS7700, Seiko Instruments, Chiba, Japan) analysis. The sintered sample (thickness: \sim 14 mm, diameter: 10 mm) was cut into a bar ($3 \times 3 \times 12 \text{ mm}^3$) and two plates ($7 \times 7 \times 2$ and $7 \times 7 \times 1 \text{ mm}^3$). A bar was used to measure the electrical conductivity and Seebeck coefficient. One plate ($7 \times 7 \times 1 \text{ mm}^3$) was used to measure the carrier concentration and mobility, and another plate ($7 \times 7 \times 2 \text{ mm}^3$) was used to measure the thermal diffusivity. The temperature-dependent Seebeck coefficient (S) and electrical resistivity (s) were measured using a ZEM-3 (ULVAC-RIKO) instrument from 313 to 764 K under He (0.1 bar). Carrier concentration (nH) and carrier mobility (μH) of the sample were measured by the Hall-effect measurement system (ResiTest8400, TOYO Co., Tokyo, Japan) with the DC four-point probe method under applying a 0.5 T magnetic field in vacuum. The thermal conductivity (κ) was calculated from the specific heat capacity (C_p), thermal diffusivity (α), and mass density (D). The α was measured from 310 to 764 K using the laser flash method (TC-1200RH, ULVAC-RIKO) under vacuum, and the D was 6.20 g cm^{-3} as determined by the Archimedes method. C_p was calculated using the Dulong–Petit law [13]. The figure of merit was calculated using the following equation: $ZT = S^2\sigma T/\kappa$.

3. Results and Discussion

3.1. Characterization of the SnTe Nanocrystal and the Sintered Sample

SEM and TEM images for the as-synthesized precipitates are shown in Figure 1a,b. Unlike the octahedral-shaped crystals of SnTe synthesized via conventional chemical methods, the precipitates are found to be spherical powders with a diameter of 14.5 ± 1.56 nm. This process is based on the charge compensation reaction between Sn^{2+} and Te^{2-} in the solution phase, which allows the rapid precipitation of nanocrystals at room temperature, suppressing crystal growth. XRD pattern of the as-synthesized precipitates are shown in Figure S1. Peaks from metallic Te and tin oxide were observed because the tiny precipitates were not stable in air and oxidized rapidly. Therefore, a subsequent annealing step is needed to obtain stable SnTe nanocrystals. The sintered sample prepared from precursors annealed below 430 K still show the existence of the metallic Te and tin oxide phase (Figure S2). On the other hand, since the sintered sample prepared from precursors annealed at 506 K was found to be a constructed single-phase SnTe (explained later), the subsequent preparation and characterization was performed for precursors annealed at 506 K.

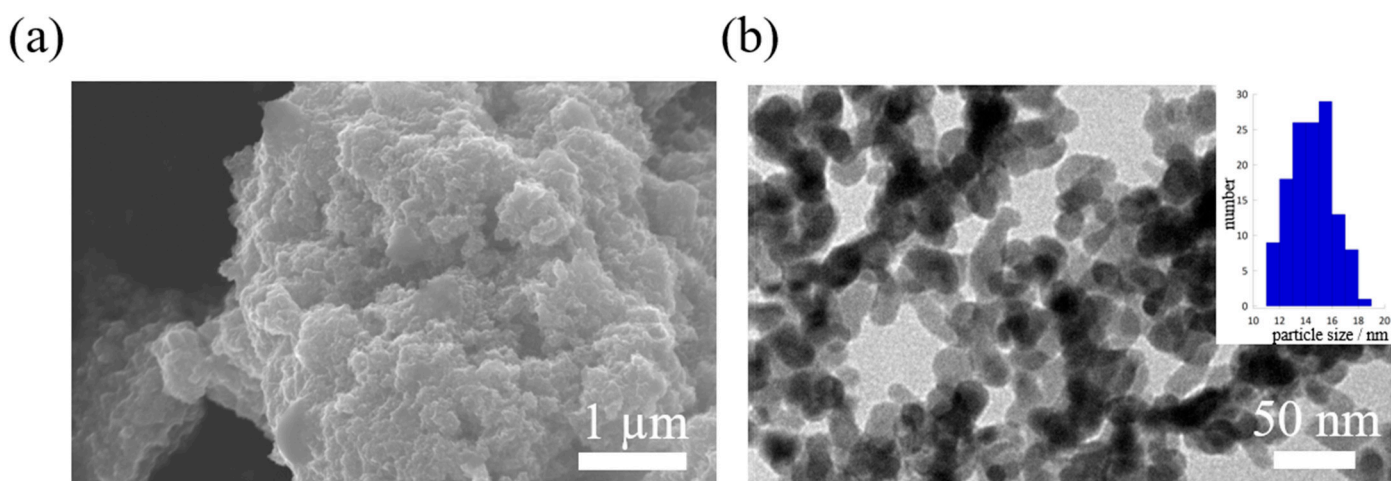


Figure 1. (a) SEM image of precipitates. The scale bar is 1 μm. (b) TEM image of precipitates and histogram of particle sizes from a survey of 158 particles. The scale bar is 50 nm.

Figure 2a shows the XRD pattern for the precursor annealed at 230 °C, where all peaks are well-indexed to fcc SnTe (PDF# 65-2945) with a space group of $Fm\bar{3}m$ and the lattice parameters of $a = b = c = 6.338$ (12) Å. These lattice parameters correspond to those of a previously reported SnTe thermoelectric alloy [15,18,38]. These results suggest that the precursor consisted of single-phase SnTe. In addition, according to the SEM image (Figure 2b), the precursor formed aggregates consisting of approximately isotropic nanoparticles with a diameter of 224 ± 52.8 nm, and the precursor (annealed nanocrystals) was grown compared to the precipitates (Figure 1a). Although further experiments are necessary, since the tiny crystals were not observed after annealing, the nanocrystals could grow via Ostwald ripening. The distribution of Sn and Te species in the precursor was examined using SEM-EDS elemental mapping, and the results are shown in Figure S3. The Sn and Te atoms were found to be homogeneously distributed throughout the nanocrystals. From these results, the present processes enable the fabrication of nanometer-scale SnTe nanocrystals without significantly including impurities.

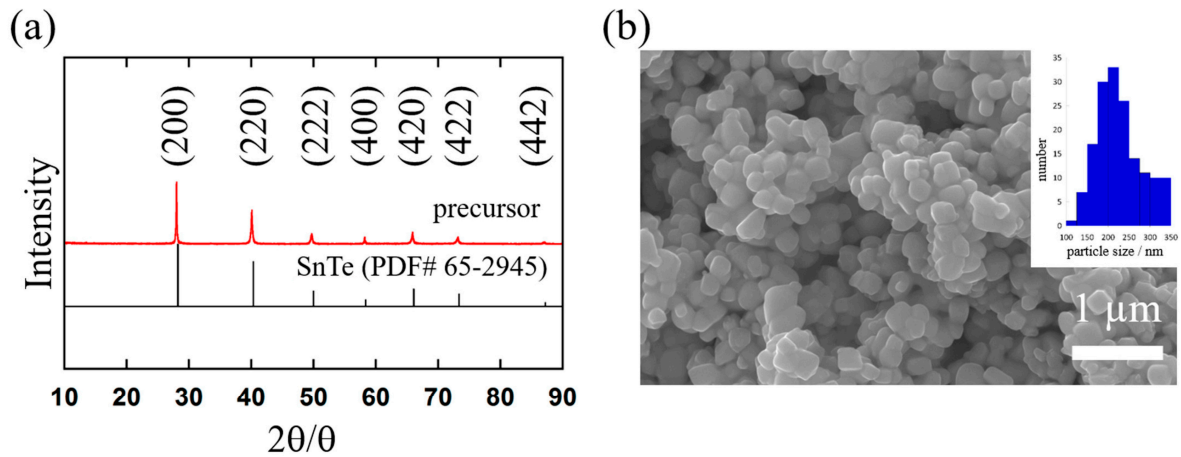


Figure 2. (a) Powder XRD pattern of the SnTe precursor. The vertical tags at the bottom are the standard diffraction patterns of octahedral SnTe (PDF# 65-2945). (b) Morphologies of the precursor detected by SEM and a histogram of particle sizes from a survey of 159 particles. The scale bar is 1 μm .

The XRD patterns of the sintered sample are shown in Figure 3a. The XRD peaks of the bulk material remain unchanged compared to the precursor (Figure 2a), and the lattice parameter calculated from them was $a = b = c = 6.339$ (13) \AA . The full width at half-maximum (FWHM) of the X-ray diffraction peaks from the (200) plane of the precursor and sintered sample were 0.141° and 0.147° , respectively, which indicates no distinct grain growth during sintering.

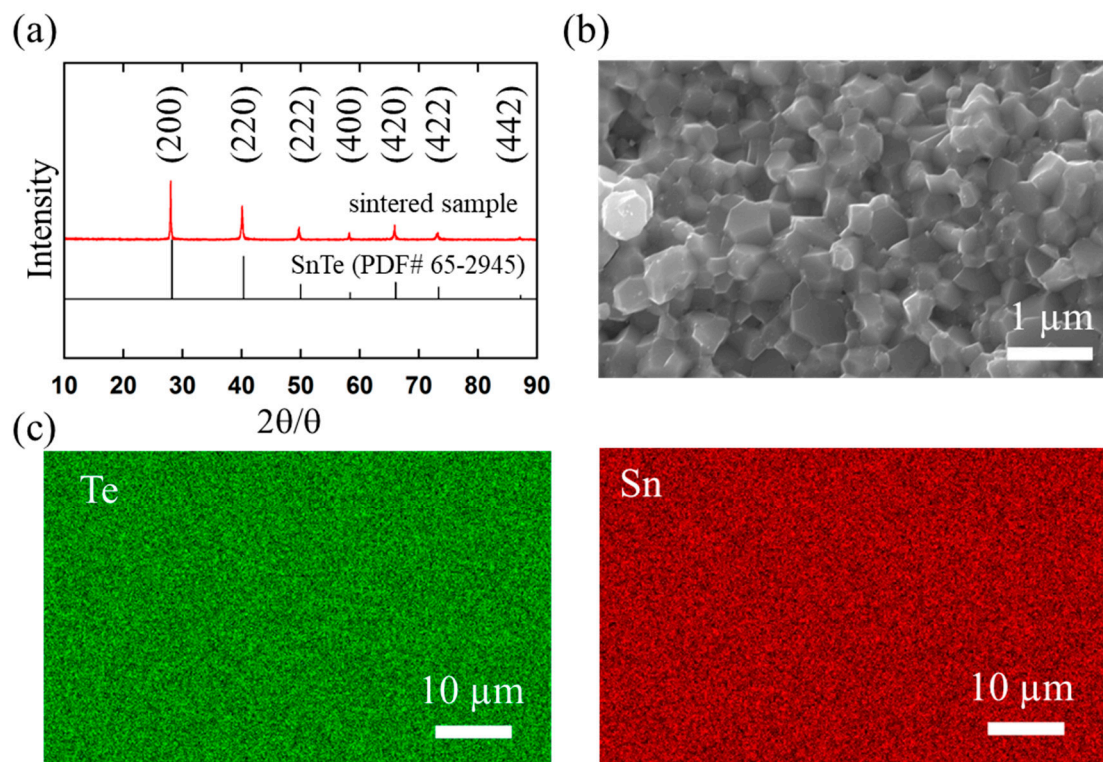


Figure 3. (a) XRD pattern of sintered SnTe sample. The vertical tags at the bottom are the standard diffraction patterns of octahedral SnTe (PDF# 65-2945). (b) Morphologies of the fractured surfaces of the sintered sample detected by SEM. The scale bar is 1 μm . (c) SEM image and EDS mapping of the sintered sample. The scale bar is 10 μm .

The internal strain rate and the average crystallite size of the sintered sample were calculated via the Williamson–Hall method from XRD data, $\beta\cos(\theta)/\lambda = 4\epsilon\sin(\theta)/\lambda + 1/D$ [39,40], where β is the integral breadth of XRD peak, θ is the X-ray diffraction angle, λ is the X-ray wavelength (Cu-K α), ϵ is the strain rate, and D is the average crystallite size, respectively. The indexed Williamson–Hall plots (plotting $\beta\cos(\theta)/\lambda$ versus $2\epsilon\sin(\theta)/\lambda$) for the sintered sample was shown in Figure S5. The straight line fitted to the plots shows that the crystallite size is 90.9 nm and the internal strain rate is 0.25%. Although it is noted that the integral breadth used for this analysis performed in this study did not take into account the instrumental contributions, including the Lorentzian and Gaussian contributions, the internal strain rate value is higher than the non-dope SnTe bulk material prepared by the melting method [39], which suggests that more defects could be introduced in the sintered sample corresponding to the bulk material [39]. Additionally, in the case of an isotropic material, calculated points should correspond to a straight line having a positive intercept (i.e., a linear function) [39], but the resulting plots did not correspond to a linear function. Therefore, although further experiments are necessary, anisotropic defects such as dislocations, stacking faults, and twinning could be introduced in the sintered sample, which could be due to the growth of crystallites from small precursors during the annealing process. These defective microstructures in the sintered sample can cause the scattering of phonons, and, therefore, a lower lattice thermal conductivity can be expected.

The SEM image of the fractured surface of the sintered sample showed a few notable defects and cracks (Figure 3b). In addition, the grains retained the original sizes and morphologies of the precursor in the sintered sample; that is, crystal growth did not occur during sintering, and the grain size remained small (100–300 nm), which can be due to the short time and high-pressure sintering. The SEM-EDS elemental mapping analysis of the sintered sample revealed a uniform distribution of Sn and Te (Figure 3c), indicating no impurity phases for the sintered sample.

The XPS spectra of the Te 3d, Sn 3d, Na 1s, B 1s, and Cl 2p regions of the sintered SnTe sample are shown in Figure S4 and were used to investigate the binding energies and chemical binding states. The spectra demonstrate no indication of elemental (metallic) tin and tellurium. The Te 3d_{3/2} and Te 3d_{5/2} peaks are observed at binding energies of 582.6 and 572.2 eV, which show the oxidation state of -2 . Further, the Sn 3d_{3/2} and Sn 3d_{5/2} peaks are observed at binding energies of 493.6 and 485.2 eV, which show the oxidation state of $+2$. The binding energies of Sn and Te agree with the reported values for Sn and Te in SnTe [41,42]. Additionally, the sintered sample include no impurity phases such as sodium, chlorine, and boron, which is consistent with the XRD results.

We have performed ICP measurements to investigate the composition and metal content of the sintered sample. The chemical composition of the sintered sample was found to be Sn_{0.988}Te_{1.000}. Since the XPS measurement showed no indication of impurity phases, the maximum concentration of Sn vacancies was estimated to be approximately 1.2%, the value of which is comparable with those of SnTe materials prepared by other methods [10]. Although further experiments are necessary, since the precipitation reaction is performed under acidic conditions, protons may be incorporated to nanocrystals instead of Sn²⁺ during the charge compensation reaction (for example, as H₂Te), which could cause the formation of a Sn vacancy through the annealing or sintering process. In addition, the metal content was calculated to be 99.9%, indicating no organic impurity phases.

3.2. Electrical Transport Properties

The electrical conductivity (σ) of the sintered sample as a function of temperature is shown in Figure 4a. σ decreased with increasing temperature from $7.07 \times 10^5 \text{ Sm}^{-1}$ at 310 K to $1.58 \times 10^5 \text{ Sm}^{-1}$ at 764 K. σ of the sintered sample was lower than that of the SnTe material prepared using melt alloying and sintering [16,43,44]. Figure 4b shows the Seebeck coefficient (S) of the sintered sample as a function of temperature; the positive S values in the measured temperature range indicate that holes are the majority carriers. The S of the sintered sample increases with increasing temperature from $41.5 \mu\text{VK}^{-1}$ at 310 K to $91.1 \mu\text{VK}^{-1}$ at 764 K. The decrease in σ and increase in S with increasing temperature

for the sintered sample are typical behaviors of degenerate semiconductors [16,45]. To evaluate detailed electrical transport properties, the temperature dependence of the carrier concentrations (nH) and mobility (μH) of the sintered sample were measured, and the results are shown in Figure 4c,d. The nH of the sintered sample was $4.88 \times 10^{20} \text{ cm}^{-3}$ at 293 K, the value of which is comparable with the carrier concentration of non-doped SnTe material with a Sn vacancy concentration of 1.56% ($4.8 \times 10^{20} \text{ cm}^{-3}$, calculated by DFT) [10]. Furthermore, the sintered sample exhibited a μH of $104 \text{ cm}^2 \text{ V}^{-1} \text{ s}^{-1}$ at 293 K; the value was significantly lower compared to those of the bulk SnTe materials [16,43]. The relationship between μH and T is generally given as follows: $\mu H \propto T^{-(1.5+r)}$ [43,46]. When $r = 0$, the charge-carrier scattering mechanism by acoustic phonons is dominant; when $r = 1$, the scattering mechanism by the interaction between acoustic and optical phonon scattering is dominant. As shown in Figure 4d, the μH for the sintered sample decreases with increasing temperature in a similar relationship to $\mu H \propto T^{(-0.5)}$ (i.e., $r = 1$), suggesting that the carrier could be scattered by grain boundaries, leading to the lower μH and σ of the sintered sample. Theoretical studies have shown that low-energy carriers with shorter relaxation times are more easily filtered out by grain boundaries than high-energy carriers with longer relaxation times, leading to relatively high Seebeck coefficients, which is known as the low-energy carrier filtering effect [47,48]. The S of the sintered sample was slightly higher than that of bulk SnTe materials with similar carrier concentrations prepared via the SHS-HG method [49], which could have been caused by the low-energy carrier filtering effect through the increased grain boundary density. Compared to the electrical transport properties of nanobulk SnTe materials prepared from nanocrystals prepared via other wet-chemical processes, such as solvothermal [15,33] and microwave methods [32], the current sintered sample exhibited a higher S and a similar or lower σ . In addition, the μH and nH values of the sintered sample were higher and similar, respectively, compared to those of the nanobulk SnTe material synthesized via solvothermal [33] and microwave methods [32]. Because the present precursor was synthesized using no organic molecules, the sintered sample could not contain organic impurities, which would serve as carrier scattering points, thereby achieving higher carrier mobility.

3.3. Thermal Transport Properties

Figure 5 plots the total and lattice thermal conductivity (κ and κ_{lat}) of the sintered sample as a function of the temperature from 310 to 765 K. The κ was calculated using the equation $\kappa = \alpha DC_p$. The density of the sintered sample was $\sim 6.20 \text{ g/cm}^3$, measured using the Archimedes method, and the relative densities of the sintered sample based on the theoretical density (6.50 g/cm^3) [50] was 95.3%. The temperature-dependent k shows a monotonically decreasing tendency with increasing temperature from $6.77 \text{ Wm}^{-1} \text{ K}^{-1}$ at 310 K to $3.24 \text{ Wm}^{-1} \text{ K}^{-1}$ at 764 K. The κ_{lat} was estimated by subtracting electronic thermal conductivity (κ_{ele}) from κ , $\kappa_{lat} = \kappa - \kappa_{ele}$ [17]. The κ_{ele} for the sintered sample was calculated using the Wiedemann–Franz law ($\kappa_{ele} = L\sigma T$) [14], where L represents the Lorenz number determined by $L = 1.5 + \exp(-|S|/116)$ [51]. The weak temperature dependence of the calculated κ_{lat} for the sintered sample demonstrates that the temperature-independent phonon scattering processes at the grain boundaries is dominant (particularly, the lattice thermal conductivity of the sintered sample from 313 to 571 K was mostly temperature-independent.) [52]. The minimum κ_{lat} of $0.87 \text{ Wm}^{-1} \text{ K}^{-1}$ was achieved at 764 K in the measured temperature range, the value of which was 50–80% of the values for bulk SnTe materials prepared using the melt alloying and sintering technique [16,43,44] and slightly lower for nanobulk materials synthesized via the solvothermal [15,33] and microwave methods [32]. The lower lattice thermal conductivity of the sintered sample is achieved probably because of the following three reasons: First, the sintered sample is formed from polydisperse SnTe grains (100–300 nm), which induce the scattering of mid- to long-wavelength phonons. Second, by decreasing the sizes of the SnTe grains, the low- and mid-frequency phonon scattering was strengthened by the densification of the grain boundary, which can be the main reason for the reduced thermal conductivity. Third,

because the SnTe precursor was synthesized via a chemical reaction, vacancies were formed in the sintered sample, which enhanced the phonon scattering to high-frequency phonons with short wavelengths [53]. Combining these effects achieved the full-spectrum scattering of phonons, leading to the low lattice thermal conductivities of the sintered sample.

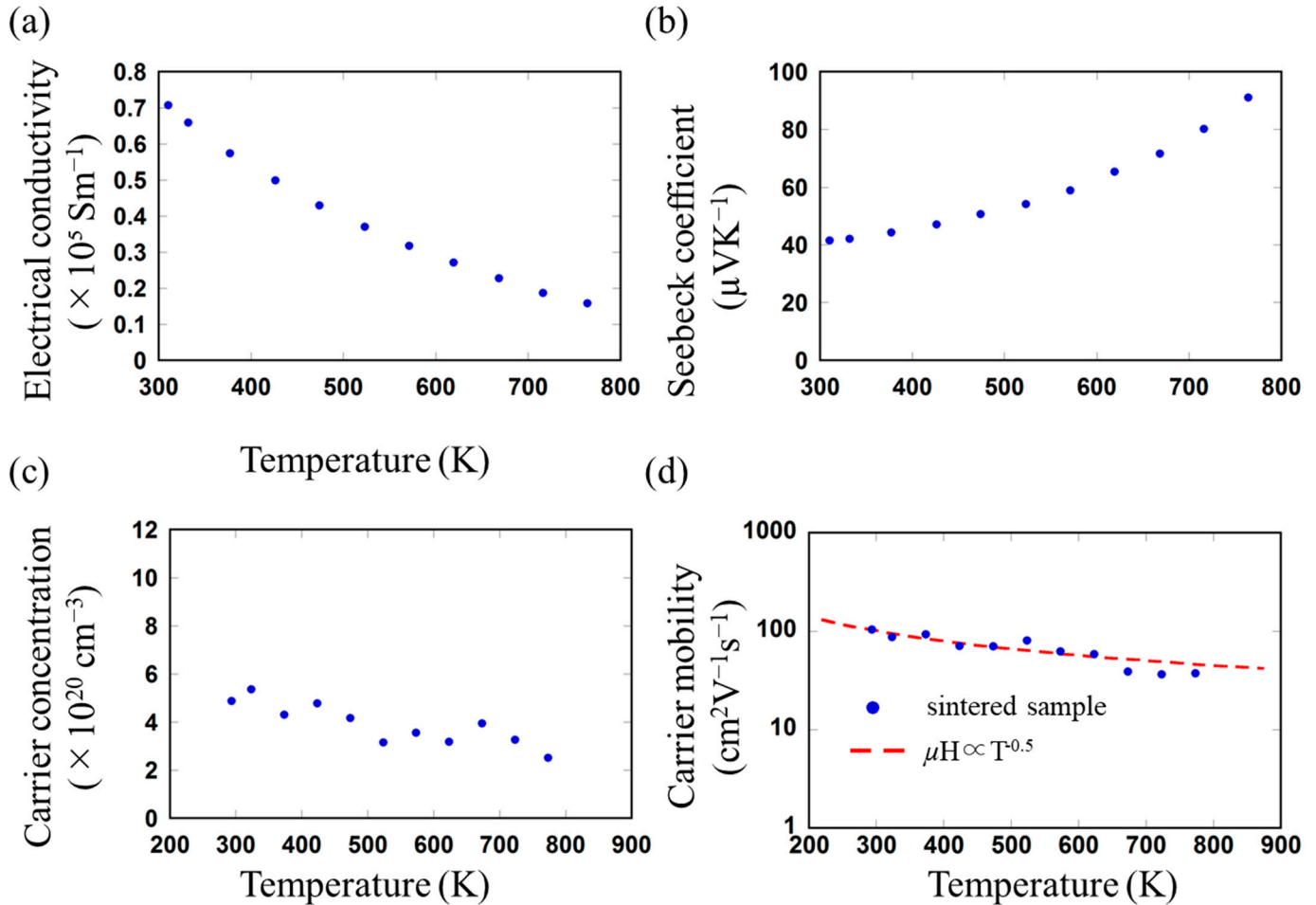


Figure 4. (a) Electrical conductivity, (b) Seebeck coefficient, (c) carrier concentration, and (d) carrier mobility as functions of sintering temperature of the SnTe sample.

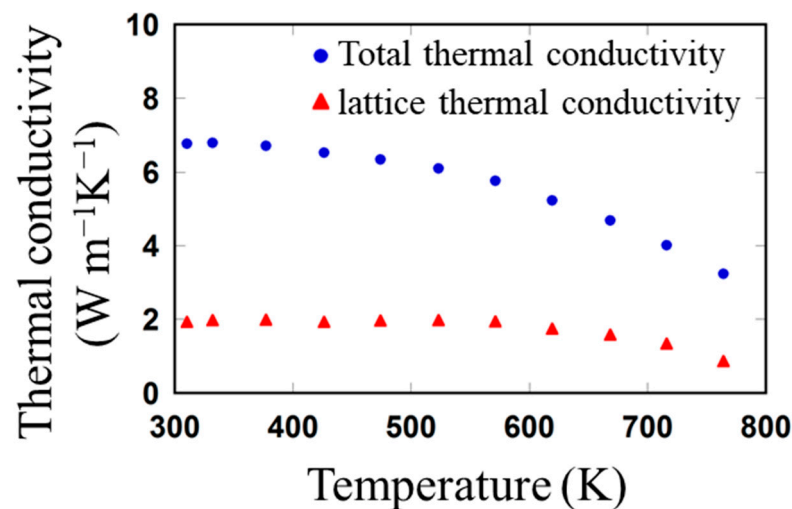


Figure 5. Temperature dependence of the total (blue) and lattice (red) thermal conductivities of the sintered SnTe material.

3.4. Figure of Merit

Figure 6 shows the variation of the ZT of the sintered sample as a function of temperature. A maximum ZT of 0.31 at 764 K was achieved. The maximum ZT of the sintered sample was comparable to those of the bulk SnTe materials prepared using the melt alloying [16,43,44], and nanobulk SnTe materials synthesized via the solvothermal [15,33] and microwave methods [32].

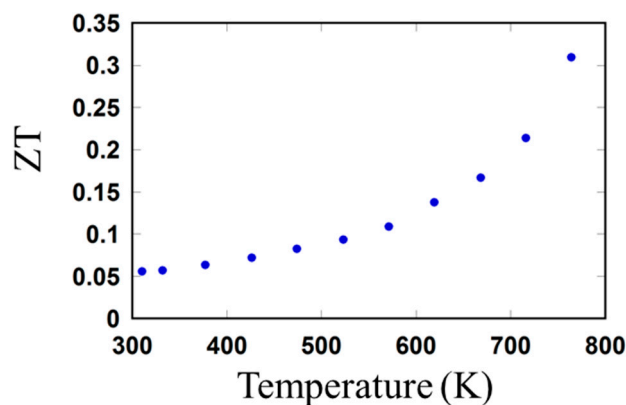


Figure 6. Temperature-dependent ZT of sintered SnTe material.

Owing to the charge compensation reaction in the solution phase, this chemical approach allows SnTe to be doped with other elements and controls its chemical composition by changing the concentration of each metal ion. Because the power factor ($PF = \sigma S^2$) for SnTe materials can be further increased without increasing the thermal conductivity by adjusting the band structure by doping with elements (e.g., Cd [19] or Mn [25], which leads to strong band convergence effects, and In [20], which introduces resonance levels in the valence band), further improvement in the thermoelectric properties of our sintered sample can be expected.

4. Conclusions

SnTe nanocrystals were successfully synthesized via chemical precipitation. The precursor was obtained by annealing the nanocrystals, and a nanostructured bulk SnTe material composed of tiny grains (100–300 nm) without impurities was prepared by sintering the precursor. The reduction in the carrier mobility of the sintered sample was relatively suppressed, which could be owing to the absence of impurities acting as carrier scattering points, and the sintered sample exhibited high electrical conductivity ($7.07 \times 10^5 \text{ Sm}^{-1}$ at 313 K). In addition, the lattice thermal conductivity of the sintered sample can be significantly reduced through the enhancement of the phonon scattering effect, presumably owing to the miniaturization of grains, achieving a low lattice thermal conductivity of $0.87 \text{ Wm}^{-1}\text{K}^{-1}$ at 764 K, thereby exhibiting a ZT of 0.31 at 764 K. In this study, we have applied chemical precipitation based on the charge compensation process to synthesize nanoscale crystals that can be further used as precursors for thermoelectric materials. This method allows for low-temperature synthesis, the rapid deposition of nanocrystals, and the control of precursor size and chemical composition through doping other impurity ions in the solution phase. Therefore, this approach demonstrates the potential to improve the thermoelectric performance of SnTe via the densification of grain boundaries, and the strategy of sintering a nanometer-scale precursor synthesized via chemical precipitation without using organic molecules could be extended to the synthesis of other multielement compounds and/or composites.

Supplementary Materials: The following supporting information can be downloaded at: <https://www.mdpi.com/article/10.3390/en17010190/s1>, Figure S1: XRD patterns of the as prepared precursors; Figure S2: XRD patterns of the sintered sample prepared from SnTe nanocrystals annealed at 430 K and 468 K; Figure S3: SEM image and EDS mapping data for the annealed SnTe nanocrystals; Figure S4: XPS spectra for Te 3d, Sn 3d, Na 1s, B 1s, and Cl 2p from the sintered SnTe sample; Figure S5: Williamson–Hall strain analysis data of the sintered SnTe sample.

Author Contributions: Methodology, R.F., T.K. and Y.T.; Investigation, R.F., Y.I. and T.T.; Writing—original draft, R.F.; Writing—review & editing, K.A. All authors have read and agreed to the published version of the manuscript.

Funding: This research received no external funding.

Data Availability Statement: Data is contained within the article and Supplementary Materials.

Conflicts of Interest: The authors declare no conflict of interest.

References

1. Hooshmand Zaferani, S.; Sams, M.W.; Shi, X.-L.; Mehrabian, N.; Ghomashchi, R.; Chen, Z.-G. Applications of Thermoelectric Generators To Improve Catalytic-Assisted Hydrogen Production Efficiency: Future Directions. *Energy Fuels* **2022**, *36*, 8096–8106. [CrossRef]
2. Channegowda, M.; Mulla, R.; Nagaraj, Y.; Lokesh, S.; Nayak, S.; Mudhulu, S.; Rastogi, C.K.; Dunnill, C.W.; Rajan, H.K.; Khosla, A. Comprehensive Insights into Synthesis, Structural Features, and Thermoelectric Properties of High-Performance Inorganic Chalcogenide Nanomaterials for Conversion of Waste Heat to Electricity. *ACS Appl. Energy Mater.* **2022**, *5*, 7913–7943. [CrossRef]
3. Tippireddy, S.; DS, P.K.; Das, S.; Mallik, R.C. Oxychalcogenides as Thermoelectric Materials: An Overview. *ACS Appl. Energy Mater.* **2021**, *4*, 2022–2040. [CrossRef]
4. Abbas, A.; Nisar, M.; Zheng, Z.H.; Li, F.; Jabar, B.; Liang, G.; Fan, P.; Chen, Y.-X. Achieving High Thermoelectric Performance of Eco-Friendly SnTe-Based Materials by Selective Alloying and Defect Modulation. *ACS Appl. Mater. Interfaces* **2022**, *14*, 25802–25811. [CrossRef] [PubMed]
5. Cao, Y.; Bai, H.; Li, Z.; Zhang, Z.; Tang, Y.; Su, X.; Wu, J.; Tang, X. Zn-Induced Defect Complexity for the High Thermoelectric Performance of n-Type PbTe Compounds. *ACS Appl. Mater. Interfaces* **2021**, *13*, 43134–43143. [CrossRef] [PubMed]
6. Tan, G.; Shi, F.; Hao, S.; Zhao, L.-D.; Chi, H.; Zhang, X.; Uher, C.; Wolverton, C.; Dravid, V.P.; Kanatzidis, M.G. Non-Equilibrium Processing Leads to Record High Thermoelectric Figure of Merit in PbTe–SrTe. *Nat. Protoc.* **2016**, *11*, 1508–1530. [CrossRef]
7. Pei, Y.; Tan, G.; Feng, D.; Zheng, L.; Tan, Q.; Xie, X.; Gong, S.; Chen, Y.; Li, J.; He, J.; et al. Integrating Band Structure Engineering with All-Scale Hierarchical Structuring for High Thermoelectric Performance in PbTe System. *Adv. Energy Mater.* **2017**, *7*, 1601450. [CrossRef]
8. Lu, X.; Lu, W.; Gao, J.; Liu, Y.; Huang, J.; Yan, P.; Fan, Y.; Jiang, W. Processing High-Performance Thermoelectric Materials in a Green Way: A Proof of Concept in Cold Sintered PbTe_{0.94}Se_{0.06}. *ACS Appl. Mater. Interfaces* **2022**, *14*, 37937–37946. [CrossRef]
9. Moshwan, R.; Yang, L.; Zou, J.; Chen, Z. Eco-Friendly SnTe Thermoelectric Materials: Progress and Future Challenges. *Adv. Funct. Mater.* **2017**, *27*, 1703278. [CrossRef]
10. Zhang, X.; Wang, Z.; Zou, B.; Brod, M.K.; Zhu, J.; Jia, T.; Tang, G.; Snyder, G.J.; Zhang, Y. Band Engineering SnTe via Trivalent Substitutions for Enhanced Thermoelectric Performance. *Chem. Mater.* **2021**, *33*, 9624–9637. [CrossRef]
11. Ma, Z.; Lei, J.; Zhang, D.; Wang, C.; Wang, J.; Cheng, Z.; Wang, Y. Enhancement of Thermoelectric Properties in Pd–In Co-Doped SnTe and Its Phase Transition Behavior. *ACS Appl. Mater. Interfaces* **2019**, *11*, 33792–33802. [CrossRef]
12. Li, W.; Wu, Y.; Lin, S.; Chen, Z.; Li, J.; Zhang, X.; Zheng, L.; Pei, Y. Advances in Environment-Friendly SnTe Thermoelectrics. *ACS Energy Lett.* **2017**, *2*, 2349–2355. [CrossRef]
13. Wang, L.; Chang, S.; Zheng, S.; Fang, T.; Cui, W.; Bai, P.; Yue, L.; Chen, Z.-G. Thermoelectric Performance of Se/Cd Codoped SnTe via Microwave Solvothermal Method. *ACS Appl. Mater. Interfaces* **2017**, *9*, 22612–22619. [CrossRef]
14. Tian, B.-Z.; Chen, J.; Jiang, X.-P.; Tang, J.; Zhou, D.-L.; Sun, Q.; Yang, L.; Chen, Z.-G. Enhanced Thermoelectric Performance of SnTe-Based Materials via Interface Engineering. *ACS Appl. Mater. Interfaces* **2021**, *13*, 50057–50064. [CrossRef]
15. Moshwan, R.; Shi, X.-L.; Liu, W.-D.; Wang, Y.; Xu, S.; Zou, J.; Chen, Z.-G. Enhancing Thermoelectric Properties of InTe Nanoprecipitate-Embedded Sn_{1-x}In_xTe Microcrystals through Anharmonicity and Strain Engineering. *ACS Appl. Energy Mater.* **2019**, *2*, 2965–2971. [CrossRef]
16. Zhou, M.; Gibbs, Z.M.; Wang, H.; Han, Y.; Xin, C.; Li, L.; Snyder, G.J. Optimization of Thermoelectric Efficiency in SnTe: The Case for the Light Band. *Phys. Chem. Chem. Phys.* **2014**, *16*, 20741–20748. [CrossRef]
17. Tan, G.; Shi, F.; Hao, S.; Chi, H.; Bailey, T.P.; Zhao, L.-D.; Uher, C.; Wolverton, C.; Dravid, V.P.; Kanatzidis, M.G. Valence Band Modification and High Thermoelectric Performance in SnTe Heavily Alloyed with MnTe. *J. Am. Chem. Soc.* **2015**, *137*, 11507–11516. [CrossRef]
18. Xu, X.; Cui, J.; Fu, L.; Huang, Y.; Yu, Y.; Zhou, Y.; Wu, D.; He, J. Enhanced Thermoelectric Performance Achieved in SnTe via the Synergy of Valence Band Regulation and Fermi Level Modulation. *ACS Appl. Mater. Interfaces* **2021**, *13*, 50037–50045. [CrossRef]

19. Tan, G.; Zhao, L.-D.; Shi, F.; Doak, J.W.; Lo, S.-H.; Sun, H.; Wolverton, C.; Dravid, V.P.; Uher, C.; Kanatzidis, M.G. High Thermoelectric Performance of P-Type SnTe via a Synergistic Band Engineering and Nanostructuring Approach. *J. Am. Chem. Soc.* **2014**, *136*, 7006–7017. [[CrossRef](#)]
20. Zhang, Q.; Liao, B.; Lan, Y.; Lukas, K.; Liu, W.; Esfarjani, K.; Opeil, C.; Broido, D.; Chen, G.; Ren, Z. High Thermoelectric Performance by Resonant Dopant Indium in Nanostructured SnTe. *Proc. Natl. Acad. Sci. USA* **2013**, *110*, 13261–13266. [[CrossRef](#)] [[PubMed](#)]
21. Banik, A.; Shenoy, U.S.; Anand, S.; Waghmare, U.V.; Biswas, K. Mg Alloying in SnTe Facilitates Valence Band Convergence and Optimizes Thermoelectric Properties. *Chem. Mater.* **2015**, *27*, 581–587. [[CrossRef](#)]
22. Banik, A.; Ghosh, T.; Arora, R.; Dutta, M.; Pandey, J.; Acharya, S.; Soni, A.; Waghmare, U.V.; Biswas, K. Engineering Ferroelectric Instability to Achieve Ultralow Thermal Conductivity and High Thermoelectric Performance in $\text{Sn}_{1-x}\text{Ge}_x\text{Te}$. *Energy Environ. Sci.* **2019**, *12*, 589–595. [[CrossRef](#)]
23. Al Rahal Al Orabi, R.; Mecholsky, N.A.; Hwang, J.; Kim, W.; Rhyee, J.-S.; Wee, D.; Fornari, M. Band Degeneracy, Low Thermal Conductivity, and High Thermoelectric Figure of Merit in SnTe–CaTe Alloys. *Chem. Mater.* **2016**, *28*, 376–384. [[CrossRef](#)]
24. Pei, Y.; Zheng, L.; Li, W.; Lin, S.; Chen, Z.; Wang, Y.; Xu, X.; Yu, H.; Chen, Y.; Ge, B. Interstitial Point Defect Scattering Contributing to High Thermoelectric Performance in SnTe. *Adv. Electron. Mater.* **2016**, *2*, 1600019. [[CrossRef](#)]
25. Wu, H.; Chang, C.; Feng, D.; Xiao, Y.; Zhang, X.; Pei, Y.; Zheng, L.; Wu, D.; Gong, S.; Chen, Y.; et al. Synergistically Optimized Electrical and Thermal Transport Properties of SnTe via Alloying High-Solubility MnTe. *Energy Environ. Sci.* **2015**, *8*, 3298–3312. [[CrossRef](#)]
26. Han, G.; Zhang, R.; Popuri, S.; Greer, H.; Reece, M.; Bos, J.-W.; Zhou, W.; Knox, A.; Gregory, D. Large-Scale Surfactant-Free Synthesis of p-Type SnTe Nanoparticles for Thermoelectric Applications. *Materials* **2017**, *10*, 233. [[CrossRef](#)]
27. Liu, T.-H.; Zhou, J.; Li, M.; Ding, Z.; Song, Q.; Liao, B.; Fu, L.; Chen, G. Electron Mean-Free-Path Filtering in Dirac Material for Improved Thermoelectric Performance. *Proc. Natl. Acad. Sci. USA* **2018**, *115*, 879–884. [[CrossRef](#)]
28. Banik, A.; Vishal, B.; Perumal, S.; Datta, R.; Biswas, K. The Origin of Low Thermal Conductivity in $\text{Sn}_{1-x}\text{Sb}_x\text{Te}$: Phonon Scattering via Layered Intergrowth Nanostructures. *Energy Environ. Sci.* **2016**, *9*, 2011–2019. [[CrossRef](#)]
29. Zhang, X.; Zhou, Y.; Pei, Y.; Chen, Y.; Yuan, B.; Zhang, S.; Deng, Y.; Gong, S.; He, J.; Zhao, L.-D. Enhancing Thermoelectric Performance of SnTe via Nanostructuring Particle Size. *J. Alloys Compd.* **2017**, *709*, 575–580. [[CrossRef](#)]
30. Ma, Z.; Wang, C.; Lei, J.; Zhang, D.; Chen, Y.; Wang, Y.; Wang, J.; Cheng, Z. Core–Shell Nanostructures Introduce Multiple Potential Barriers to Enhance Energy Filtering for the Improvement of the Thermoelectric Properties of SnTe. *Nanoscale* **2020**, *12*, 1904–1911. [[CrossRef](#)]
31. Peng, P.; Wang, C.; Li, L.; Li, S.; Chen, J.; Fan, P.; Du, R.; Si, H.; Cheng, Z.; Wang, J. Enhanced Thermoelectric Performance of In-Doped and AgCuTe-Alloyed SnTe through Band Engineering and Endotaxial Nanostructures. *Phys. Chem. Chem. Phys.* **2022**, *24*, 27105–27113. [[CrossRef](#)]
32. Wang, L.; Hong, M.; Sun, Q.; Wang, Y.; Yue, L.; Zheng, S.; Zou, J.; Chen, Z.-G. Hierarchical Structuring to Break the Amorphous Limit of Lattice Thermal Conductivity in High-Performance SnTe-Based Thermoelectrics. *ACS Appl. Mater. Interfaces* **2020**, *12*, 36370–36379. [[CrossRef](#)]
33. Liu, X.; Zhang, B.; Chen, Y.; Wu, H.; Wang, H.; Yang, M.; Wang, G.; Xu, J.; Zhou, X.; Han, G. Achieving Enhanced Thermoelectric Performance in $(\text{SnTe})_{1-x}(\text{Sb}_2\text{Te}_3)_x$ and $(\text{SnTe})_{1-y}(\text{Sb}_2\text{Se}_3)_y$ Synthesized via Solvothermal Reaction and Sintering. *ACS Appl. Mater. Interfaces* **2020**, *12*, 44805–44814. [[CrossRef](#)]
34. Wang, L.; Zheng, S.; Chen, H. Enhanced Electronic Transport Properties of Se-Doped $\text{SnTe}_{1-x}\text{Se}_x$ Nanoparticles by Microwave-Assisted Solvothermal Method. *J. Electron. Mater.* **2017**, *46*, 2847–2853. [[CrossRef](#)]
35. Ibáñez, M.; Hasler, R.; Genç, A.; Liu, Y.; Kuster, B.; Schuster, M.; Dobrozhan, O.; Cadavid, D.; Arbiol, J.; Cabot, A.; et al. Ligand-Mediated Band Engineering in Bottom-up Assembled SnTe Nanocomposites for Thermoelectric Energy Conversion. *J. Am. Chem. Soc.* **2019**, *141*, 8025–8029. [[CrossRef](#)]
36. Fujiwara, R.; Takashima, Y.; Tsuruoka, T.; Naito, M.; Murai, J.; Akamatsu, K. Chemical Synthesis of Single Nanometer-Sized $\text{Bi}_{2-x}\text{Sb}_x\text{Te}_{3.0}$ Nanocrystals via Direct Precipitation Process. *Results Chem.* **2022**, *4*, 100485. [[CrossRef](#)]
37. Fujiwara, R.; Takashima, Y.; Tsuruoka, T.; Naito, M.; Murai, J.; Akamatsu, K. High-Performance Bulk $\text{Bi}_{0.4}\text{Sb}_{1.6}\text{Te}_{3.0}$ Thermoelectrics Prepared from Nanocrystal Precursor Synthesized via Chemical Precipitation. *J. Solid State Chem.* **2023**, *319*, 123777. [[CrossRef](#)]
38. Aminzare, M.; Tseng, Y.-C.; Ramakrishnan, A.; Chen, K.-H.; Mozharivskiy, Y. Effect of Single Metal Doping on the Thermoelectric Properties of SnTe. *Sustain. Energy Fuels* **2019**, *3*, 251–263. [[CrossRef](#)]
39. Muchtar, A.R.; Srinivasan, B.; Tonquesse, S.L.; Singh, S.; Soelami, N.; Yuliarto, B.; Berthebaud, D.; Mori, T. Physical Insights on the Lattice Softening Driven Mid-Temperature Range Thermoelectrics of Ti/Zr-Inserted SnTe—An Outlook Beyond the Horizons of Conventional Phonon Scattering and Excavation of Heikes’ Equation for Estimating Carrier Properties. *Adv. Energy Mater.* **2021**, *11*, 2101122. [[CrossRef](#)]
40. Williamson, G.K.; Hall, W.H. X-ray Line Broadening from Filled Aluminium and Wolfram. *Acta Metall.* **1953**, *1*, 22–31. [[CrossRef](#)]
41. Shalvoy, R.B.; Fisher, G.B.; Stiles, P.J. Bond Ionicity and Structural Stability of Some Average-Valence-Five Materials Studied by X-ray Photoemission. *Phys. Rev. B* **1977**, *15*, 1680–1697. [[CrossRef](#)]
42. Neudachina, V.S.; Shatalova, T.B.; Shtanov, V.I.; Yashina, L.V.; Zyubina, T.S.; Tamm, M.E.; Kobeleva, S.P. XPS Study of SnTe(100) Oxidation by Molecular Oxygen. *Surf. Sci.* **2005**, *584*, 77–82. [[CrossRef](#)]

43. Li, W.; Chen, Z.; Lin, S.; Chang, Y.; Ge, B.; Chen, Y.; Pei, Y. Band and Scattering Tuning for High Performance Thermoelectric $\text{Sn}_{1-x}\text{Mn}_x\text{Te}$ Alloys. *J. Mater.* **2015**, *1*, 307–315. [[CrossRef](#)]
44. Mandava, S.; Basu, R.; Khasimsaheb, B.; Bathula, S.; Muthukumar, V.S.; Singh, A.; Neeleshwar, S. A Synergistic Approach to Achieving the High Thermoelectric Performance of La-Doped SnTe Using Resonance State and Partial Band Convergence. *Mater. Adv.* **2021**, *2*, 4352–4361. [[CrossRef](#)]
45. Tan, H.; Guo, L.; Wang, G.; Wu, H.; Shen, X.; Zhang, B.; Lu, X.; Wang, G.; Zhang, X.; Zhou, X. Synergistic Effect of Bismuth and Indium Codoping for High Thermoelectric Performance of Melt Spinning SnTe Alloys. *ACS Appl. Mater. Interfaces* **2019**, *11*, 23337–23345. [[CrossRef](#)]
46. Hasezaki, K.; Hamachiyo, T.; Ashida, M.; Ueda, T.; Noda, Y. Thermoelectric Properties and Scattering Factors of Finely Grained Bi_2Te_3 -Related Materials Prepared by Mechanical Alloying. *Mater. Trans.* **2010**, *51*, 863–867. [[CrossRef](#)]
47. Gayner, C.; Amouyal, Y. Energy Filtering of Charge Carriers: Current Trends, Challenges, and Prospects for Thermoelectric Materials. *Adv. Funct. Mater.* **2020**, *30*, 1901789. [[CrossRef](#)]
48. Heremans, J.P.; Thrush, C.M.; Morelli, D.T. Thermopower Enhancement in PbTe with Pb Precipitates. *J. Appl. Phys.* **2005**, *98*, 063703. [[CrossRef](#)]
49. Su, H.; Han, Y.; Xie, L.; Jiang, M.; Wang, Z.; Miao, Z.; Liu, G.; Zhou, M.; Huang, R.; Li, L. Fast Fabrication of SnTe *via* a Non-Equilibrium Method and Enhanced Thermoelectric Properties by Medium-Entropy Engineering. *J. Mater. Chem. C* **2023**, *11*, 5363–5370. [[CrossRef](#)]
50. Li, Z.; Chen, Y.; Li, J.-F.; Chen, H.; Wang, L.; Zheng, S.; Lu, G. Synthesizing SnTe Nanocrystals Leading to Thermoelectric Performance Enhancement via an Ultra-Fast Microwave Hydrothermal Method. *Nano Energy* **2016**, *28*, 78–86. [[CrossRef](#)]
51. Kim, H.-S.; Gibbs, Z.M.; Tang, Y.; Wang, H.; Snyder, G.J. Characterization of Lorenz Number with Seebeck Coefficient Measurement. *APL Mater.* **2015**, *3*, 041506. [[CrossRef](#)]
52. Mehta, R.J.; Zhang, Y.; Karthik, C.; Singh, B.; Siegel, R.W.; Borca-Tasciuc, T.; Ramanath, G. A New Class of Doped Nanobulk High-Figure-of-Merit Thermoelectrics by Scalable Bottom-up Assembly. *Nat. Mater.* **2012**, *11*, 233–240. [[CrossRef](#)] [[PubMed](#)]
53. Vineis, C.J.; Shakouri, A.; Majumdar, A.; Kanatzidis, M.G. Nanostructured Thermoelectrics: Big Efficiency Gains from Small Features. *Adv. Mater.* **2010**, *22*, 3970–3980. [[CrossRef](#)] [[PubMed](#)]

Disclaimer/Publisher’s Note: The statements, opinions and data contained in all publications are solely those of the individual author(s) and contributor(s) and not of MDPI and/or the editor(s). MDPI and/or the editor(s) disclaim responsibility for any injury to people or property resulting from any ideas, methods, instructions or products referred to in the content.